Journal of Materials Chemistry A

Accepted Manuscript

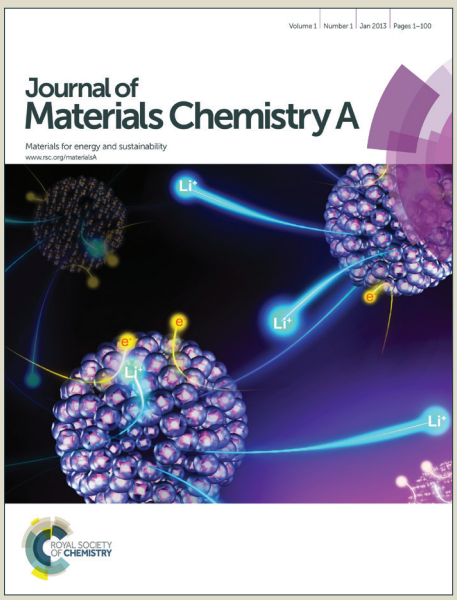

ROYAL SOCIETY OF CHEMISTRY

www.rsc.org/materialsA

Piperidinium Tethered Nanoparticle-hybrid Electrolyte for Lithium Metal Batteries

Kevin S. Korf,‡ Yingying Lu,‡ Yu Kambe, Lynden A. Archer*

[*] School of Chemical and Biomolecular Engineering, Cornell University, Ithaca, NY 14853-5201 Email: laa25@cornell.edu

[‡] These authors contribute equally to this work.

Abstract

We report on the synthesis of novel piperidinium-based ionic liquid tethered nanoparticle hybrid electrolytes and investigate their physical and electrochemical properties. Hybrid electrolytes based on the ionic liquid 1-methyl-3-propypiperidinium bis(brifluoromethanesulfone) imide covalently tethered to silica nanoparticles (SiO_2-PP-TFSI) were blended with propylene carbonate/1M lithium bis(brifluoromethanesulfone) imide (LiTFSI). We employed NMR analysis to confirm the successful creation of the hybrid material. Dielectric and rheological measurements show that these electrolytes exhibit exceptional room-temperature DC ionic conductivity (10^{-2} to 10^{-3} S/cm) as well as high shear mechanical moduli (10^5 to 10^6 Pa). Lithium transference numbers were found to increase with particle loading and to reach values as high as 0.22 at high particle loadings where the particle jam to form a soft glassy elastic medium. Analysis of lithium electrodeposits obtained in the hybrid electrolytes using SEM and EDX spectra show that the SiO_2-PP-TFSI nanoparticles are able to smooth lithium deposition and inhibit lithium dendrite proliferation in Li metal batteries. LTO|SiO_2-PP-TFSI/PC in 1M LiTFSI|Li half-cells based on the SiO_2-PP-TFSI hybrid electrolytes exhibit attractive voltage profiles and trouble-free extended cycling behavior over more than 1000 cycles of charge and discharge.

Introduction

Research into new materials compositions and electrode designs for rechargeable lithium batteries has received considerable attention in recent years. This interest can be credited to growing awareness that lithium-ion battery (LiB) technology is approaching its theoretical performance limits and only incremental advances are likely for the foreseeable future as the various cell components and packaging are optimized for performance and cost. This situation can be contrasted with the steadily rising performance & safety targets and sophistication of power sources needed to power new engineered systems, such as autonomous aircraft, hybrid and electric vehicles, robotics, and portable electronics.[1-4] Rechargeable lithium batteries that utilize metallic lithium as the anode predate LiB technology,[5-6] now in widespread use in portable electronics and have always been understood to offer such superior storage capacities, on either a gravimetric or volumetric basis, to demand careful attention. Appropriately protected lithium metal can also be used for aqueous rechargeable lithium batteries (ARLBs) to obtain superfast charging [7] and high energy density [8]. Additionally, because such *lithium metal batteries* (LMBs) contain an abundant supply of lithium in the anode, they open the way for various unlithiated cathode configurations, such as elemental sulfur in lithium-sulfur batteries[2] or air in lithium-air batteries,[3] which offer impressive enhancements in storage relative to today's LiB technology.

The lithiated graphitic carbon anode (LiC_6) in currently marketed lithium ion batteries has a gravimetric capacity of approximately 360 mA h g^{-1}.[1,9] Disposing of the inactive carbon host in the anode can boost the overall storage capacity as much as ten-fold, to yield a theoretical capacity of 3860 mA h g^{-1}.[4,10] In combination with a suitable high-energy anode material (e.g. O_2 in a Li-air battery) an overall specific energy of up to 11,140 Wh kg^{-1}, comparable to that of many fossil fuels is theoretically possible, a goal that is ideal for multiple applications in transportation.[11] The propensity of metallic lithium to form unstable, arborescent/dendritic metal

electrodeposits over repeated cycles of charge and discharge presents a significant practical barrier that must be overcome for widespread commercial deployment of any of these lithium metal battery configurations. This dendritic growth eventually spans the electrodes and results in short circuit of the cell.[2] The ohmic heat generated by the short circuit may lead to rapid overheating of the electrolyte, which may present serious fire and explosion hazards.[12] Lithium ion batteries are designed to remove this risk by storing lithium in its ionic state. However, a potential of less than 100 mv separates lithium ion insertion in a graphitic carbon host from lithium plating onto a lithium metal surface, meaning that if a Li-ion cell is charged too fast or overcharged, metallic lithium deposits may accumulate in the anode and dendrites can form by similar processes as for a LMB.

Chazalviel et al.[13-14] and Newman et al.[15-16] have proposed theoretical frameworks that provide good starting points for understanding the nucleation and proliferation of metal dendrites during recharge of LMBs. Chazalviel and his coworkers solved the one-dimensional electromigration/diffusion problem for the concentration of ions and electric field in a polarized cell and concluded that uneven lithium deposition begins when a region of unbalanced charge/*space charge* forms in the vicinity of the lithium anode due to depletion of anions in the electrolyte. They determined that the time-scale for formation of the space charge is the Sands time in the electrolyte, a strong decreasing function of the current density at the electrode and an increasing function of the lithium ion transference number and the ionic conductivity of the electrolyte. The rate at which a nucleated dendrite front propagates from the space charge region was also shown to be proportional to the anion drift velocity in the electrolyte.[14]

Both predictions imply that an electrolyte in which anions are fixed in space and their spatial distribution maintained uniform during cell polarization might cycle dendrite free. A recent stability analysis that captures these physics and which balances the dendrite-forming tendency of the flux concentration produced by the space charge, with suppression due to surface tension

shows that while dendrites may still grow in such a structured electrolyte, the growth rate can be significantly reduced by tethering even a fraction (O(10%)) of the anions.[17] Several earlier reports have addressed strategies for creating such structured electrolytes, in which only lithium cations are mobile,[18-21] or in which anions ionically tethered to nanoparticles uniformly distributed in a gel electrolyte serve as an anion reservoir that can be released and supplied to neutralize the space charge in response to the high local electric fields created by charge imbalance near the anode. Galvanostatic polarization and electrochemical cycling studies show that both types of electrolytes produce an order of magnitude improvement in lifetime of lithium metal cells cycled at moderate rates.

The analysis of Monroe and Newman takes a different posture. In this approach, the dendrites are assumed to be always present, but the dendrites grow in response to a balance of forces that include surface tension and mechanics of the electrolyte.[15] A formal stability analysis led these authors to conclude that the stability of a lithium metal electrode with respect to dendrite growth is a much stronger function of the shear modulus of the electrolyte and the magnitude of compressive forces at the electrolyte/electrode interface than to surface tension. A key consequence of this analysis is that a solid-state electrolyte with shear mechanical modulus approximately twice that of metallic lithium (4 GPa at room temperature; negligible at 180.5 ^{o}C) is predicted to be sufficient to completely stabilize the electrode/electrolyte interface and prevent dendrite proliferation in a LMB.[15-16] This means that a hard solid electrolyte (no cracks) or a chemically or physically cross-linked, semi-solid polymer electrolyte that is stable at the melting temperature of lithium would be good candidates for stabilizing the interface and stopping dendrite growth. Additionally, the authors reported that for a solid electrolyte of any modulus, application of compressive forces to the electrolyte is a much more effective procedure for stabilizing the interface than increasing the electrolyte surface tension. Finally, the analysis shows that the dendrite growth rate increases as the dendrite propagates and increasing the

cation transference number increased the charge passed before short circuit, enhancing the cell lifetime.

Previous experimental studies suggest other methods to suppress or prevent dendritic growth in LMBs while maintaining essential cell properties. Alloyed lithium anodes such as lithium-sodium and lithium-potassium have been studied with some success for reducing dendrite growth, but the alloys lower the energy density able to be achieved in the cell.[22,23] Electrolytes that utilize physical barriers comprised of high moduli ceramic materials have been employed to prevent dendritic growth.[24] These electrolytes often exhibit low conductivities and are prone to cracking during cell assembly and to poor adhesion and cracking problems between the electrolyte and the electrodes due to the large volume changes in the lithium anode during cycling.[25] A recent promising approach employs a nanoporous alumina filled with a conventional carbonate liquid electrolyte to achieve electrolytes with both attractive mechanical properties and ion transport characteristics.[26] By laminating these electrolytes with a flexible, macroporous fluorinated polymer, the authors further showed that it is possible to impart mechanical toughness. These so-called nanoporous hybrid electrolytes have been shown to lead to exceptionally stable cycling behavior in both symmetric and ½ cell LMBs for more than 500 charge/discharge cycles at low to moderate current densities. SEI additives have been used to improve the elasticity of the SEI layer.[27] Finally, electrolytes comprised of nanoparticle salts with cation transference numbers approaching unity have recently been proposed for extending cell lifetimes in LMBs.[18,19]

Ionic liquids have also been widely studied as electrolytes for lithium metal batteries due to their below room temperature melting point, negligible vapor pressure, thermal and electrochemical stability, and non-flammability.[28-30] They have been shown to enable safe operation of lithium batteries at moderate rates. Among room temperature ionic liquids, piperidinium based fluids have shown greatest potential for use in lithium battery applications.

Studies in lithium-ion batteries have also shown that a piperidinium based ionic liquid with 10 wt% vinylene carbonate can maintain 90% of its initial capacity after 100 cycles.[31] Piperidinium ionic liquids paired with a charge delocalized bis(trifluoromethylsulfonyl)imide anion, or TFSI, anion have electrochemical stabilities of around 6V, as compared to others, such as ionic liquids based on imidazolium with stabilities of 4.3V vs lithium electrode.[30,32] 1-Methyl-1-propylpiperidinium paired with a TFSI anion (PP13-TFSI) has been reported to exhibit ionic conductivities around 1.51 mS cm^{-1} and a higher Coulombic efficiency than the equivalent pyrrolidinium based ionic liquids (P13-TFSI) when cycled in a Li/LiTFSI and IL-TFSI/$LiCoO_2$ cell.[33] Liu et al. demonstrated that the addition of 1.44 moles of PP13-TFSI into a polymer electrolyte system comprised of 1 mol of PEO_{18}LiTFSI can lower the interfacial resistance in the SEI by up to a factor of 5, which effectively lowers the overpotential for lithium plating/stripping.[11]

Recently Lu et al. reported that by covalently tethering ILs to inorganic nanoparticles, it is possible to achieve electrolytes with excellent mechanical tunability, ionic conductivity, and electrochemical stability in LMBs.[20,21,34] The inorganic cores in these materials are thought to act as anchor points for the ILs and when used at high loadings in conjunction with a supporting salt (e.g. LiTFSI) in an electrolyte, these nanoparticle tethered ILs have been shown to lead to electrolytes[34] or ILs with no detectable melting transition.[35] At a certain threshold particle loading unique to each system, the electrolytes transition to a jammed, semi-solid state in which each nanoparticle is surrounded by “cages” formed by its neighbors, creating a network where the particles are no longer able to freely explore phase space. These “cages” are associated with an energy threshold that must be overcome in order to rearrange the material. This jamming phenomenon allows the material to simultaneously exhibit solid-like moduli as well as liquid-like transport properties.[36-38]

Piperidinium tethered silica nanoparticle hybrid electrolyte (SiO_2-PP-TFSI) with propylene carbonate (PC) and 1M LiTFSI are studied here for their high ionic conductivities, lithium transference numbers, and MPa scale storage moduli. The ability of the SiO_2-PP-TFSI SEI layer to promote smooth electrodeposition of lithium is demonstrated. Finally, cycled cells containing the SiO_2-PP-TFSI electrolyte reveal excellent cyclability without short circuit.

Experimental

Synthesis

1-methyl piperdine and 3-chloropropyl trimethoxysilane, commercially available from Sigma-Aldrich, were dissolved in DMF in a 1 : 1.2 molar ratio and stirred in a sealed environment at 80°C for 2 days. The reaction product was washed with ether 3 – 4 times to remove any unreacted materials and impurities. The ether was evaporated off the remaining product to obtain the 1-methyl-1-propyl piperidinium chloride with the trimethoxysilane tail. The 1-methyl-1-propyl piperidinium chloride with the silane tail was reacted with SM30 LUDOX, 30% 10 nm silica nanoparticles by weight in aqueous suspension, in a 1: 2.2 weight ratio in deionized water at 100 °C for 12 hours. Approximately 2 mL of hydrochloric acid was added to the solution to bring the pH down to 2 in order to facilitate leaving of hydroxyl groups on the silica surface and attachment of the silane group. The 1-methyl-1-propyl piperidinium chloride with the silane tail was added in two equal steps throughout the reaction, once initially and once 6 hours into the synthesis. The resultant product was then washed with a 60/40 methanol/ether cosolvent to allow the nanoparticles precipitate out of solution. The piperidinium functionalized nanoparticles and solvent were centrifuged at 8000 rpm for 20 minutes to separate solvent, unreacted materials, and ionic liquid-functionalized nanoparticles. Top layer of excess solvent and unreacted materials was removed and the IL-functionalized nanoparticles were lyophilized in a freeze dryer to allow the remaining traces of solvent to evaporate, leaving only the chlorinated tethered particle (SiO_2-PP-Cl) as the product. A 1:1.5 weight ratio of the SiO_2-PP-Cl product

and LiTFSI were dissolved separately in deionized water and the LiTFSI / DI water solution was slowly added to the SiO_2-PP-Cl solution with continuous stirring. An immediate reaction was observed and due to the hydrophobic nature of the TFSI anion, the final tethered particle (SiO_2-PP-TFSI) product precipitated out of solution. The tethered particle was separated from water through centrifugation and freeze dried to evaporate residual water and to obtain the pure tethered particle powder. A schematic is shown in Scheme 1 to illustrate the synthesis steps.

To make the final electrolyte solutions, a predetermined amount of tethered particle powder was redissolved in acetone and stirred for 1 day to achieve a fully dissolved solution. A calculated 1M LiTFSI and different proportions of PC were then added to the dissolved SiO_2-PP-TFSI. The sample was dried by convection oven at 50°C for 3 days and the final traces of solvent were removed by drying in a vacuum oven at 45°C for 12 hours. The final electrolytes of several different particle loadings were kept in an argon glovebox for use.

Analysis Methods

The ionic conductivity was measured using a Novocontrol N40 broadband dielectric spectrometer. Rheology measurements were performed with a Paar Physica MCR 501 with 10mm and 25mm cone diameters with a tip angle of 1-4 degrees. NMR was performed in an INOVA 400 using VNMRJ 1.1B and VNMR 6.1C software. The lithium transference number was measured at room temperature by Solartron frequency response analyzer (model 1252). SEM images were taken using a LEO 1550-FESEM in conjunction with EDX to determine surface compositions of the SEI layer. SEM samples were prepared from post-mortem symmetric coin cells. Coin cells were polarized at a fixed current density (0.006-0.2mA/cm^2) until short-circuit observed, dissembled in a glove box filled with inert argon gas and the lithium anode extracted. The anode was washed in PC to remove any tethered electrolyte that was not contained in the SEI layer. The sample was then evacuated in the glove box antechamber to evaporate the

remaining propylene carbonate for 3 hours until dry. Following evaporation the samples were placed into a small plastic container sealed with parafilm to prevent oxidation during transport to the SEM facility. Cycling experiments were performed using half cell batteries with LTO/glass fiber + tethered electrolyte/Li setups, respectively, in a battery cycler (Neware CT-3008). All cells were made in an argon filled glovebox with oxygen and water levels below 10 ppm. LTO spinel nanopowder with particle size larger than 100nm, super P carbon black, and polyvinylidene difluoride were mixed in a 8:1:1 weight ratio in N-methylpyrrolodone. The resulting slurry was coated on copper foil using a film casting doctor blade (MTI Corp.) and dried in a vacuum oven for 12 hours.

Results and Discussion

Composition analysis of 1-methyl-1-propyl piperidinium chloride with the silane tail by proton NMR spectroscopy shows peaks in all the expected locations. The peaks in Figure 1 confirm that synthesis of the ionic liquid with the silane tail was successful. Several small peaks displayed are traced back to solvents used during synthesis or residual cleaning solvents, all labeled accordingly in Figure 1. The peak at 3.2 represents the CH_3 of methanol created from the hydrolyzation of the methyl groups of h*, the * denoting different degrees of methylization. It is noteworthy that several peaks are affected by the different degrees of the methylization off of the methoxysilane group. The peaks labeled a, h*, and g in Figure 1a all display a step down of three different peak heights of varying chemical shifts that can be seen in Figures 1b and 1c. This suggests that there could be one, two, or three methyl groups off the silane tail. Since there are no peaks for an ionic liquid with zero methyl groups, it can be concluded that these were washed away during purification. Interestingly, the fact that the degree of methylization of h* affects the chemical shift of the methyl group labeled “g” provides some insight into the conformation of the ionic liquid. This may indicate that the “g” side of the ionic liquid could be

folding back on itself, causing the methyl group g to be much more affected by what is attached to the silane than the illustration suggests.

Conductivity measurements in Figure 2 show values ranging from 6 x 10^{-4} to 5 x 10^{-3} S/cm at room temperature that inversely correlate with particle loading. The material with the highest particle loading exhibits a ten-fold decrease in conductivity; a factor of 15 increase in mechanical modulus in the low strain un-yielded state (Fig. 3a); and more than a three orders of magnitude enhancement in modulus post yield. This represents an uneven trade-off between conductivity and mechanical strength that can be manipulated to determine a particle loading that will optimize processing of the IL-composite electrolytes, mechanical properties of the electrolyte in cells, and maintain the necessary conductivity for proper battery performance.

The solid lines through the data in Figure 2 are best fit curves obtained using the VFT expression for temperature-dependent DC conductivity: $\sigma = A\exp(-B/(T-T_0))$, where σ is DC conductivity, A is the pre-exponential factor, B represents the effective activation energy for coupled ions and local segmental motion, and T and T_0 are the measurement and reference temperatures, respectively. Parameters from VFT fitting were shown in Table S1. In this case the reference temperature was taken as the glass transition temperature obtained by DSC analysis. A VFT form that properly fits the data infers that the conductivity stems from local chain relaxation, segmental motion, and electrolyte crystallinity.[39] The extra mobility of the chains that have one end free is thought to allow for exaggerated swinging motion that is able to aid ion movement through the electrolyte medium that has a more distinct impact on conductivity at lower temperatures. This swinging is related to the glass transition temperature and the swinging has a greater effect the higher the operating temperature is above the glass transition temperature. This causes the effect to be more pronounced at lower temperatures in the electrolytes with the lowest glass transition temperatures. At the highest temperatures, ionic motion is dominated more by the solvation sphere and transition state for ionic motion, which is

more consistent across particle loadings, resulting in a more compact data set at higher temperatures.

It can also be seen from the data that the addition of nanoparticles themselves insignificantly affects the conductivity, but rather the resultant increase in viscosity caused by these nanoparticles that reduces the conductivity. An increase in viscosity is known to cause a decrease in the free volume in the electrolyte and diminishes available pathways for ions to move through the electrolyte, ultimately resulting in a significant decrease in conductivity. Kim et al. reported a pure 1-methyl-3-propylimidazolium TFSI ionic liquid with an ionic conductivity of 7.42 x 10^{-3} S/cm at 30 °C dropped to 1.17 x 10^{-3} S/cm and a pure 1-methyl-1-butylpyrrolidinium TFSI dropped from 3.77 x 10^{-3} to 8.67 x 10^{-5} when the viscosity was increased by a 1:1 molar ratio addition of LiTFSI.[40] The conductivity of the nanoparticle-free control solution in Figure 2b shows that the conductivity is consistently high with minimal change in conductivity over a chain loading range from 11% to 48%. In addition, comparison of the 11% particle loading electrolyte to the control solution without the IL-nanoparticle (PC and 1M LiTFSI) shows an almost perfect overlap of the data, indicating that the nanoparticles themselves have negligible detrimental effect on the conductivity at low particle loading.

The lithium transference number was estimated by the method attributed to Bruce and Scrosati.[41] The lithium transference number represents the portion of the ionic conductivity that is due to lithium transport and can be estimated as:

$$T_{Li^+} = \frac{I_{ss}(\Delta V - I_0 R_0)}{I_0(\Delta V - I_{ss} R_{ss})}$$

where T_{Li}^+ is the lithium transference number, I_0 and I_{ss} are the initial and steady state currents of a cell undergoing a polarization potential of ΔV, and R_0 and R_{ss} are the interfacial resistances before and after polarization. The cell resistance and current is measured before the cell is

polarized to obtain reference points of the electrolyte as a whole. When the cell is completely polarized the TFSI anions are driven to one electrode while the lithium cations, which have a source from which to strip and a sink to deposit, are transported freely to the opposite electrode. When fully polarized, only lithium ions are thought to contribute to the measured current.

Using this method, it was found that the piperidinium tethered electrolyte with 11%, 23%, and 48% particle loadings exhibit lithium transference numbers that increase with particle loading, T_{Li}^{+} of 0.04±0.02, 0.11±0.02, and 0.22±0.02 respectively (see supporting information Figure S1), likely reflecting the lower contribution of the particle-tethered ILs to conduction as the electrolytes traverse the jamming transition. Lithium transference numbers in the range 0.1 - 0.25 are typical in ionic liquid systems (0.2 for systems of imidazolium and pyrrolidinium based ionic liquids with TFSI as the counterion) [42-44], but are usually lower than polymer-based systems [45,46]. Here, the initial current used in this analysis was calculated from the relationship, $I_0 = \Delta V / (R_{bulk} + R_{interface})$. The relatively low lithium transference number could lead to high ion concentration gradient, thereby increasing the possibility of localized ion depletion and unstable electrodeposition.[17] However, current understanding is that ionic liquids might form stable SEI compared with conventional liquid electrolytes, which promotes reversible lithium striping and plating at the electrode and creates uniform electrodeposits.[20,21] Therefore, in terms of piperidinium-based ILs, accelerating lithium ion transport in the interface appears more important for stabilizing electrodeposition than increasing the T_{Li}^{+}.

Results in Figure 3a and 3b show that the storage modulus G' of the composite electrolytes measured in shear flow exceeds the loss modulus, G'', at almost all particle loadings studied. This means that the materials are all viscoelastic fluids and respond in a more solid-like manner to mechanical perturbations than conventional liquid electrolytes. The maximum exhibited in the loss modulus for higher particles loadings is characteristic of a

jammed material in which each SiO_2 nanoparticle is thought to be encaged by neighboring particles, enhancing the materials elasticity. At a critical applied shear strain, mechanical forces imposed on the material are large enough to break the cages, which causes it to yield, flow, and dissipate mechanical energy as the individual particles move relative to each other and contribute viscous friction. As with other such jammed nanoparticle hybrid materials, the transition is accompanied by a characteristic loss (G'') maximum at shear strains coincident with the yield point.[38,47-49] The G'' hump begins to disappear in electrolytes with particle loading around 41% and is completely absent in systems with 36% loading; indicating that the caging effects become less important at lower particle concentrations. At shear strains above the yield point, the material exhibits strain-softening, plastic flow where both moduli decrease and the loss modulus ultimately overtakes the storage modulus as the material begins to exhibit liquid-like rheology.

Post-mortem analysis of the lithium electrode of symmetric coin cells after failure by polarization (supporting information Figure S2) shows a cracked lithium surface with rougher electrodeposits in the cavities between cracks, while other areas appear to be smooth and unaffected by dendrites. It is theorized that uneven deposition of lithium metal produces seeds for lithium dendrite growth, and the tip of the dendrite during growth is led by a depletion zone that draws additional lithium ions in to deposit.[13-14] Energy Dispersive X-Ray Spectroscopy (EDX) was performed in tandem with SEM to analyze the chemical make-up of the rough and smooth regions of the post-mortem samples. Figure 4b shows EDX of the dendritic and smooth regions of the electrode along with the corresponding SEM image of the area of the electrode under investigation. EDX performed on the dendritic region showed only peaks of oxygen and carbon. Lithium is known to readily oxidize when exposed to air and the larger oxygen peak is a result of a combination of lithium oxidation and the oxygen found in the propylene carbonate additive. The carbon peak is purely from the residual propylene carbonate left on the lithium anode after

the anode was dried. EDX performed on the smooth region, however, shows a spectrum that contain large peaks in carbon, oxygen, fluorine, silicon, and a small nitrogen peak just below .40 keV, obtained from an SEI layer containing the silica nanoparticle tethered to the piperidinium ionic liquid with the TFSI anion. This data along with the SEM images show that an SEI layer containing the tethered electrolyte is able to smooth lithium deposition and prevent puncturing by dendritic growth. It is possible this is due to the combination of mechanical suppression from the rigid particle network within the SEI layer that acts as a physical barrier and the lower overpotential for lithium plating and stripping that is unique to the piperidinium system. However, as it can be seen that lithium dendrites are still able to propagate through cracks, it is not yet enough to say that this smoothing of lithium deposition is enough to completely prevent dendritic growth, but what is clear from the data is that it is facilitated by the SiO_2-PP-TFSI particles in the electrolyte.

Galvanostatic cycling experiments were performed on full cell batteries with lithium titanate (LTO)/glass fiber + tethered electrolyte/Li setup. The LTO cathode contained 5% vapor grown carbon fiber and 5% carbon black. LTO has a theoretical capacity of 175 mAh/g and is known to undergo negligible structural changes during lithium insertion/deinsertion processes and to operate stably at high current densities in conventional liquid alkyl carbonate electrolytes.[50-51] It has been reported that the particular cathode configuration used here exhibits a 20% improvement in capacity over LTO electrodes that solely contained either of the two carbon materials.[52] Two high-conductivity hybrid electrolytes containing 11vol% and 23vol% SiO_2 particles was used for this component of the study. A fixed rate of 3C, calculated using based on the theoretical capacity of LTO, was used for all of the experiments discussed herein.

Figure 5 reports on the voltage profiles and cycling characteristics of Li/LTO half-cells containing our SiO_2-PP-TFSI composite electrolytes (also see supporting information Figure S3). Figure 5(a) shows that an electrolyte with ϕ=0.11 exhibits stable charge discharge profiles over

1000 cycles of charge and discharge. Both composite electrolytes, ϕ=0.11 and ϕ=0.23, exhibit attractive capacity retention over at least 1200 cycles and retain coulombic efficiencies close to 90% after 1000 cycles. Notably, even after the capacity fade at high cycle numbers, after 2000 cycles of charge and discharge, the cells retain 63% and 50% of ther initial capacity. Capacity fade in many lithium batteries occur during overcharge or overdischarge and are associated with decomposition of the electrolyte, lithium dissolution, and passive film formation.[53] SEI formation is known to occur within the first few cycles, consistent with the initial capacity loss in both electrolytes. It is also noteworthy that even after 2000 cycles in both the 11% and 23% tethered electrolyte cells as shown in graph S2, the cycling profiles displayed no sign of short circuit or premature cell failure. This further demonstrates the electrolyte's ability to facilitate stable electrodeposition of lithium and to resist dendrite growth in a battery. Hurdling this major obstacle that has plagued lithium metal batteries is a major step forward. This paired with the large capacity retention exhibited by the cycled cells underscore the importance of composite electrolytes based on piperidinium tethered nanoparticles for future work.

Conclusions

We have created piperidinium-tethered ionic-liquid silica nanoparticles and used them to create composite electrolytes in a liquid, propylene carbonate - 1M LiTFSI host. NMR analysis of the ionic-liquid hybrid nanoparticles confirms their chemistry and suggests that the untethered piperidinium chloride ionic liquid exhibits folded structures that are suppressed upon tethering to nanoparticles. Conductivity and rheological measurements reveal that even at high particle contents high room temperature ionic conductivities in the 10^{-4} to 10^{-3} S/cm range can be achieved in gel-like electrolytes that simultaneously exhibit mechanical shear moduli in the 10^5 to 10^6 Pa range and jamming. Lithium transference numbers were found to increase with particle loading and relatively high (for piperidinium ILs) transference numbers (T_{Li}^+ = 0.22) can be achieved at a particle loading of 48 vol%.

Previous electrochemical analysis of the electrolytes in extended lithium plate-strip experiments in Li/Li symmetric cells reveal that they exhibit remarkable ability to extend cell lifetimes by stabilizing lithium electrodeposition and preventing lithium dendrite proliferation.[21] Interrogation of the electrodes using SEM in conjunction with EDX show that the SiO_2-PP-TFSI particles are in fact selectively adsorbed in regions where smooth lithium deposits are observed. Half-cell galvanostatic cycling experiments using an LTO|SiO_2-PP-TFSI/PC in 1M LiTFSI|Li exhibit attractive capacity retention with minimal electrolyte degradation for over 1000 cycles of charge and discharge. These cells also show no evidence of premature failure by Li dendrite nucleation and growth during repeated cycles of charge and discharge.

Acknowledgements

This work was supported by the National Science Foundation, Award No. DMR-1006323 and by Award No. KUS-C1-018-02, made by King Abdullah University of Science and Technology (KAUST). Facilities available though the Cornell Center for Materials Research (CCMR) were used for this study (DMR-1120296). The authors thank Dr. Ivan Keresztes for the help with the NMR analysis.

References

1. J.-M. Tarascon and M. Armand, *Nature*, 2001, **414**, 359.
2. B. Jin, J.-U. Kim and H.-B. Gu, *J. Power Sources*, 2003, **117**, 148.
3. G. Girishkumar, B. McCloskey, A. C. Luntz, S. Swanson and W. Wilcke, *J. Phys. Chem. Lett.*, 2010, **1**, 2194.
4. M. Armand and J.-M. Tarascon, *Nature*, 2008, **451**, 652.
5. M.S. Whittingham, *Science*, 1976. **192**, 1126.
6. A. Yoshino, *Angew. Chem. Int. Ed.*, 2012, **51**, 5798.

7. W. Tang, Y. Zhu, Y. Hou, L. Liu, Y. Wu, K. P. Loh, H. Zhang and K. Zhu, *Energy Environ. Sci.*, 2013, **6**, 2093.

8. Y. Hou, X. Wang, Y. Zhu, C. Hu, Z. Chang, Y. Wu and R. Holze, *J. Mater. Chem. A,* 2013, **1**, 14713.

9. P. G. Bruce, S. A. Freunberger, L. J. Hardwick and J.-M. Tarascon, *Nature*, 2011, **11**, 19.

10. P. G. Bruce, B. Scrosati and J.-M. Tarascon, *Angew. Chem. Int. Ed.*, 2008, **47**, 2930.

11. S. Liu, N. Imanishi, T. Zhang, A. Hirano, Y. Takeda, O. Yamamoto and J. Yang, *J. Electrochem. Soc.*, 2010, **157**, A1092.

12. D. Aurbach, E. Zinigrad, C. Yaron and H. Teller, *Solid State Ionics*, 2002, **148**, 405.

13. J.-N. Chazalviel, *Phys. Rev. A.*, 1990, **42**, 7355.

14. C. Brissot, M. Rosso, J.-N. Chazalviel and S. Lascaud, *J. Power Sources*, 1999, **81-82**, 925.

15. C. Monroe and J. Newman, *J. Electrochem. Soc.*, 2005, **152**, A396.

16. C. Monroe and J. Newman, *J. Electrochem. Soc.*, 2003, **150**, A1377.

17. M.D. Tikekar, L.A. Archer, and D.L. Koch, *J. Electrochem. Soc.,* 2014, **161***,* A847

18. J. L. Schaefer, D. Yanga and L. A. Archer, *Chem. Mater.*, 2013, **25,** 834.

19. S. Srivastava, J. L. Schaefer, Z. Yang, Z. Tu and L. A. Archer, *Adv. Mater.*, 2014, **26**, 201.

20. Y. Lu, S. K. Das, S. S. Moganty and L. A. Archer, *Adv. Mater.*, 2012, **24**, 4430.

21. Y. Lu, K. Korf, Y. Kambe, Z. Tu and L. A. Archer, *Angew. Chemie. Int Ed.*, 2014, **53**, 488.

22. J. K. Stark, Y. Ding and P. A. Kohl, *J. Electrochem. Soc.*, 2011, **158**, A1100.

23. J. A. Vega, J. Zhou and P. A. Kohl, *J. Electrochem. Soc.*, 2009, **156**, A253.

24. L. Gireaud, S. Grugeon, S. Laruelle, B. Yrieix and J.-M. Tarascon, *Electrochem. Comm.*, 2006, **8**, 1639.

25. G. M. Stone, S. A. Mullin, A. A. Teran, D. T. Hallinan Jr., A. M. Minor, A. Hexemer and N. P. Balsara, *J. Electrochem. Soc.*, 2012, **159**, A222.

26. Z. Tu, Y. Kambe, Y. Lu, and L. A. Archer, *Adv. Energy Mater.*, 2014, **4**, 1300654.

27. G. A. Umeda, M. Richard, K. L. Stamm, F. Wudl and B. Dunn, *J. Mater. Chem.*, 2011, **21**, 1593.

28. G. H. Lane, P. M. Bayley, B. R. Clare, A. S. Best, D. R. Macfarlane, M. Forsyth and A. F. Hollenkamp, *J. Phys. Chem. C*, 2010, **114**, 21775.

29. B. Scrosati and J. Garche, *J. Power Sources*, 2010, **195**, 2419.

30. A. Lewandowski, A. and A. S. Widerska-Mocek, *J. Power Sources*, 2009, **194**, 601.

31. A. Lewandowski, A. and A. S. Widerska-Mocek, *J. Power Sources*, 2007, **171**, 938.

32. M. Galinski, A. Lewandowski and I. Stepniak, *Electrochim. Acta*, 2006, **51**, 5567.

33. H. Sakaebe and H. Matsumoto, *Electrochem. Commun.*, 2003, **5**, 594.

34. Y. Lu, S. S. Moganty, J. L. Schaefer and L. A. Archer, *J. Mater. Chem.*, 2012, **22**, 4066.

35. S.S. Moganty, S. Srivastava, Y. Lu, J.L. Schaefer, S. Rizvi and L.A. Archer, *Chem. Materials* 2012, **24**, 1386

36. P. Sollich, F. Lequeux, P. Hébraud and M. E. Cates, *Phys. Rev. Lett.*, 1997, **78**, 2020

37. S. S. Moganty, N. Jayaprakash, J. L. Nugent, J. Shen and L. A. Archer, *Angew. Chem.*, 2010, **122**, 9344

38. J. L. Nugent, S.S. Moganty, D. A. Yanga, and L. A. Archer, *J. Materials Chem.* 2011, **21**, 10094

39. J. B. Kerr, S. E. Sloop, G. Liu, Y. B. Han, J. Hou and S. Wang, *J. Power Sources*, 2002, **110**, 389.

40. J.-K. Kim, A. Matic, J.-H. Ahn and P. Jacobsson, *J. Power Sources*, 2010, **195**, 7639.

41. P. G. Bruce, J. Evans and C. A. Vincent, *Solid State Ionics*, 1988, **28-30**, 918.

42. S. Duluard, J. Grondin, J.-L. Bruneel, I. Pianet, A. Grélard, G. Campet, M.-H. Delville and J.-C. Lassègues, *J. Raman Spectrosc.*, 2008, **39**, 627.

43. Y. Saito, T. Umecky, J. Niwa, T. Sakai and S. Maeda, *J. Phys. Chem. B*, 2007, **111**, 11794.

44. T. Frömling, M. Kunze, M. Schönhoff, J. Sundermeyer and B. Roling, *J. Phys. Chem. B.*, 2008, **112**, 12985.

45. Y. Zhu, F. Wang, L. Liu, S. Xiao, Z. Chang and Y. Wu, *Energy Environ. Sci.,* 2013, **6**, 618.

46. M. Wetjen, G.-E. Kim, M. Joost, G. B. Appetecchi, M. Winter, S. Passerini*, J. Power Sources,* 2014, **246**, 846.]

47. J.L. Nugent, S.S. Moganty and L.A. Archer, *Adv. Materials*, 2010, **22**, 3677

48. P. Agrawal, S. Srivastava and L.A. Archer, *Phys. Rev. Lett.* 2011, **107**, 268302

49. S. Srivastava, J. H. Shin and L.A. Archer, *Soft Matter*, 2012, **8**, 4097

50. K. Nakahara, R. Nakajima, T. Matsushima and H. Majima, *J. Power Sources*, 2003, **117**, 131.

51. K. Sawai, R. Yamato and T. Ohzuku, *Electrochim. Acta*, 2006, **51**, 1651.

52. Y. Kambe, A. J. Fernandez and L. A. Archer, *Mater. Res. Soc. Symp. Proc.*, 2013, **1541**.

53. P. Arora, R. E. White and M. Doyle, *J. Electrochem. Soc.*, 1998, **145**, 3657.

Table of Contents Graphic

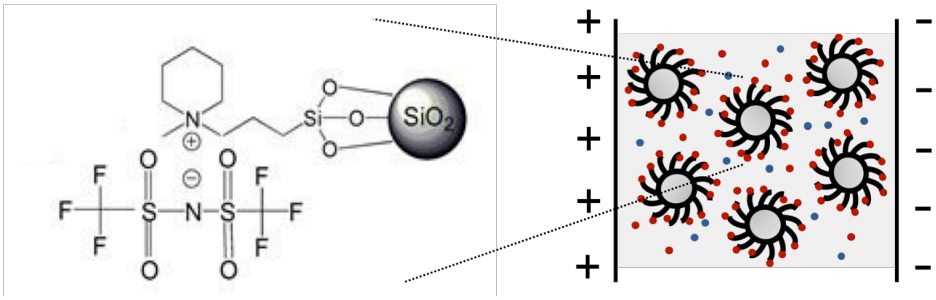

Piperidinium-based ionic liquid hybrid nanoparticle electrolytes exhibit exceptional ionic conductivity and smoothen lithium electrodeposition during recharge of lithium metal batteries.

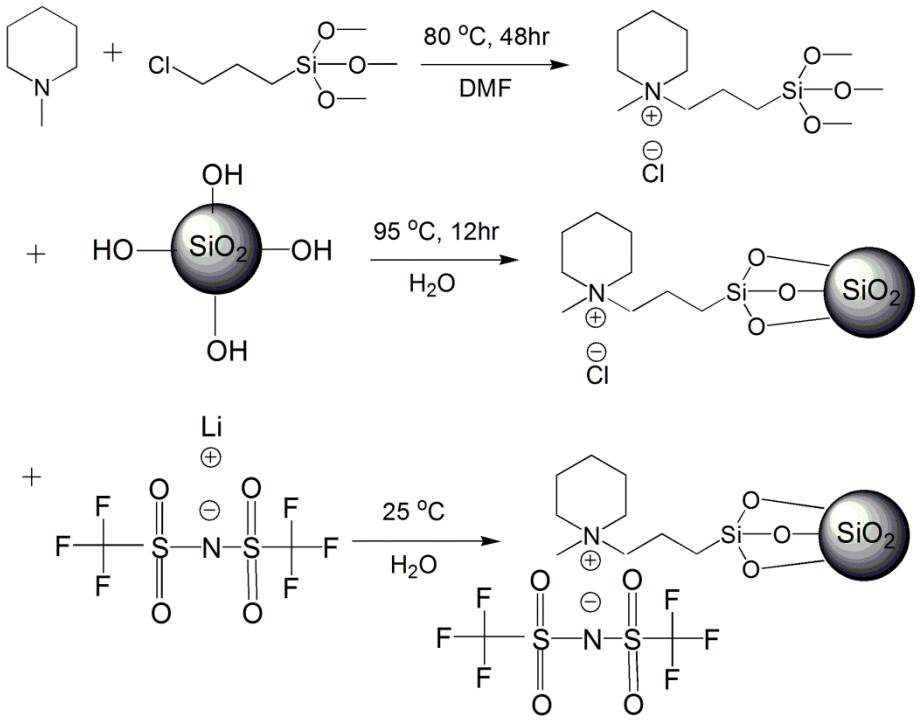

Scheme 1: Synthesis method used for preparing SiO_2-PP-TFSI.

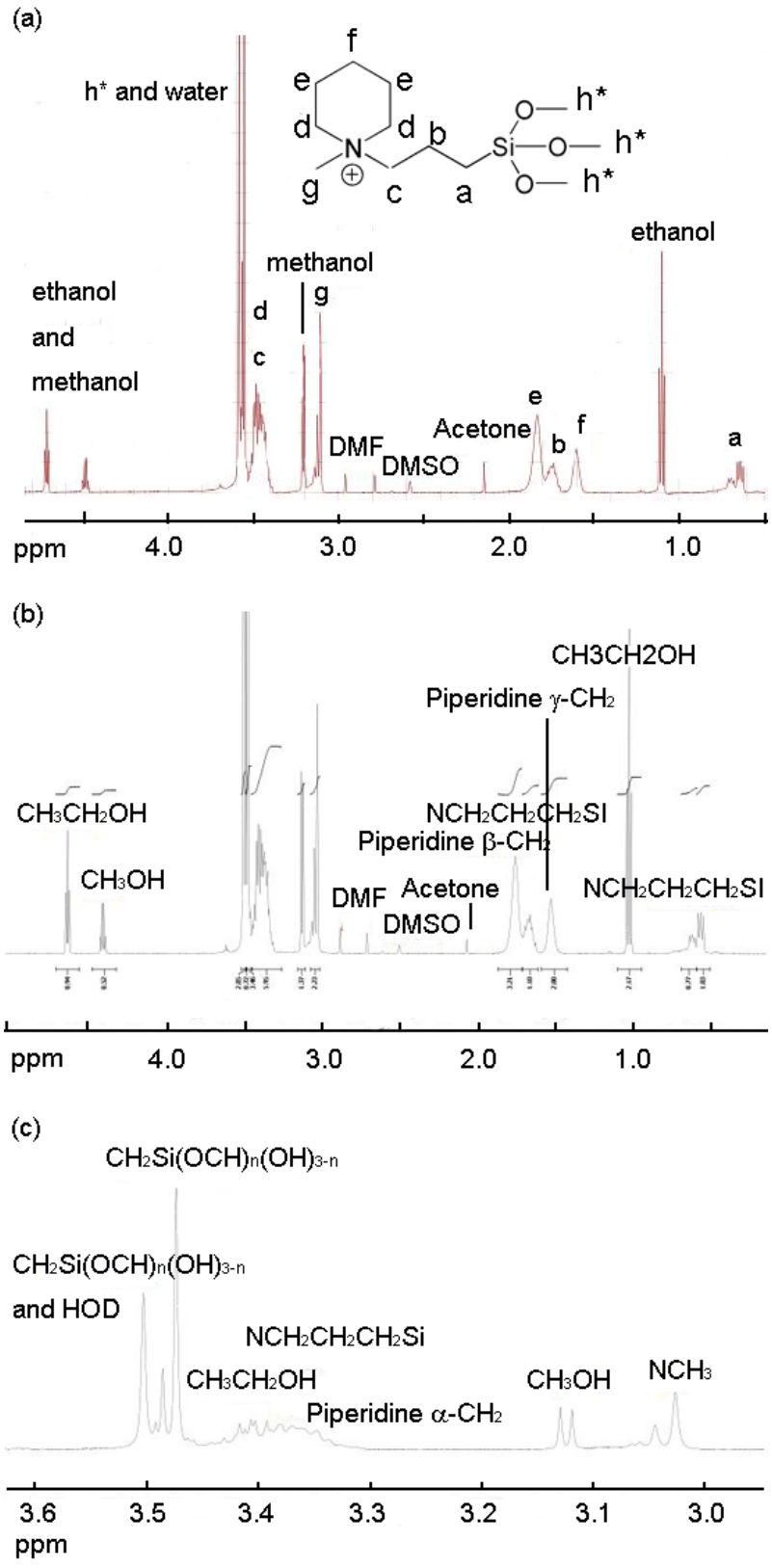

Figure 1: (a) Peaks labeled corresponding to each proton NMR active group in the piperidinium ionic liquid; (b) Detailed labeling of peaks showing step down caused by different degrees of methylization of the silane tail; (c) Enlarged view of groups with chemical shifts between 2.9 and 3.6 ppm.

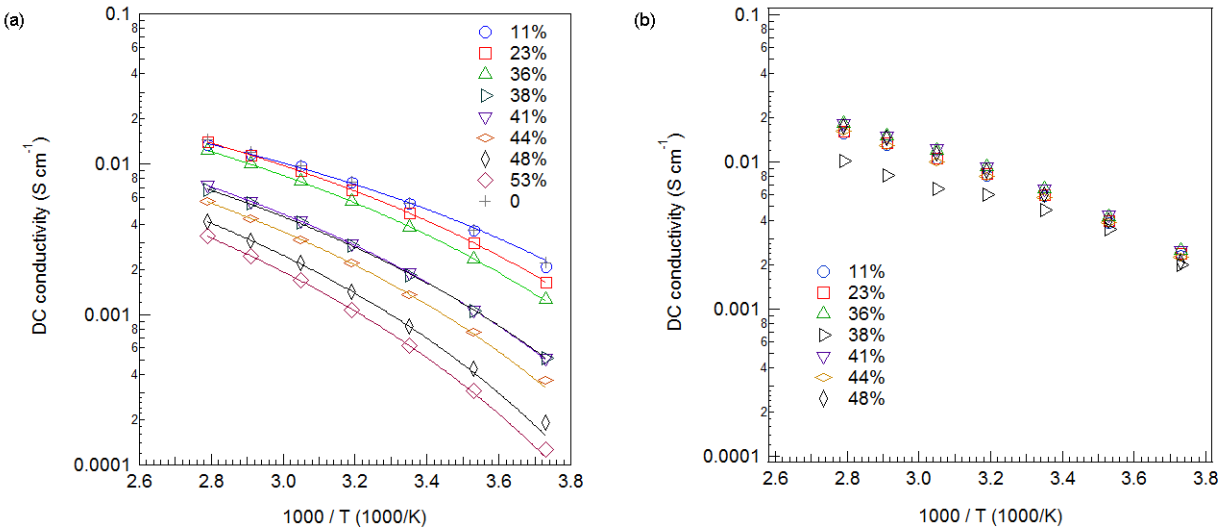

Figure 2: DC conductivities as a function of temperature for (a) SiO2-PP-TFSI and (b) PP-TFSI at various SiO_2 nanoparticle loadings.

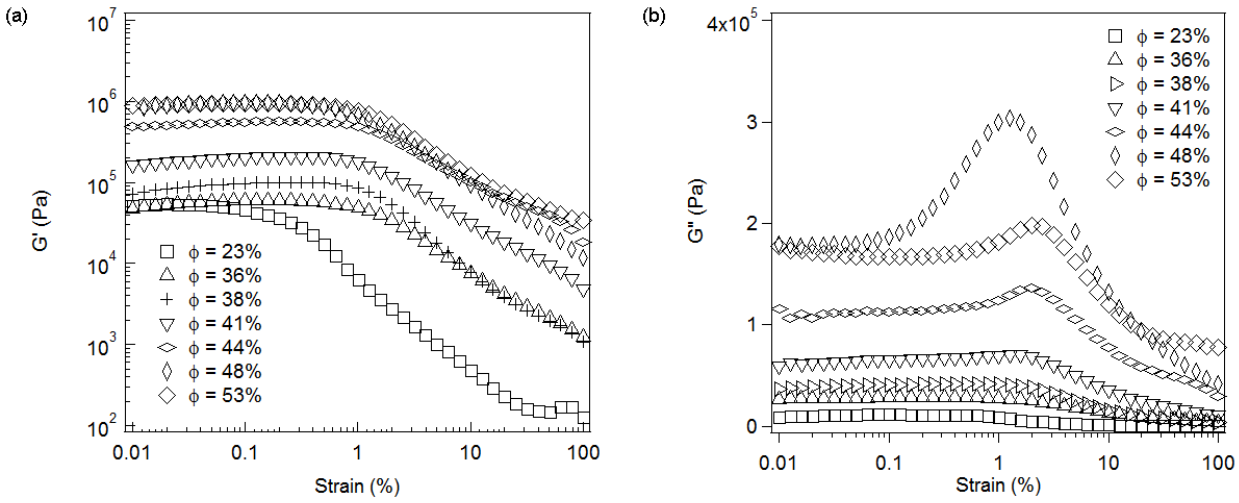

Figure 3: (a) Dynamic storage (G') and (b) loss (G'') moduli for hybrid electrolytes as a function of SiO_2-PP-TFSI loading and shear strain. Measurements were performed at 25 ^{o}C and a fixed angular frequency of 5rad/s.

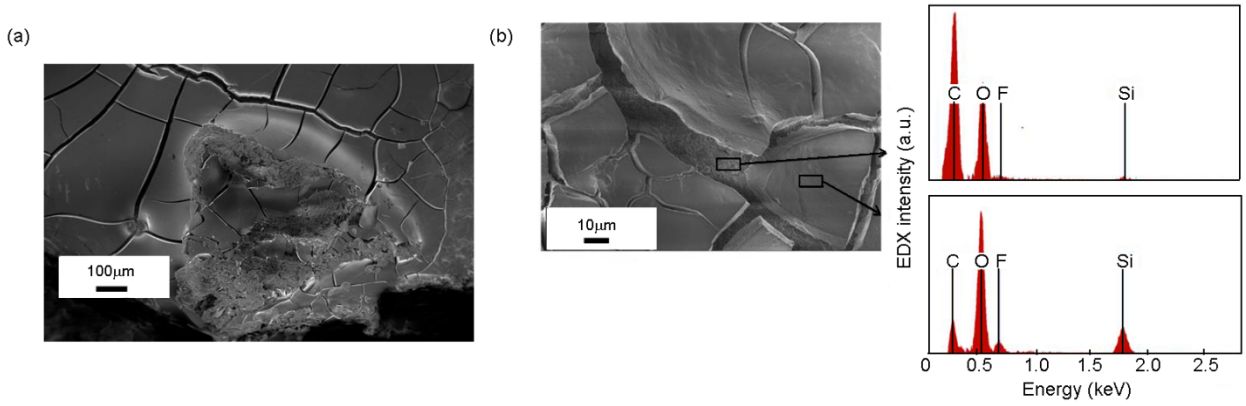

Figure 4: (a) SEM analysis of lithium anode in ϕ=0.36 Li|SiO_2-PP-TFSI|Li cell after short-circuit by galvanostatic polarization. (b) EDX analysis for smooth region and rough region of the corresponding SEM image.

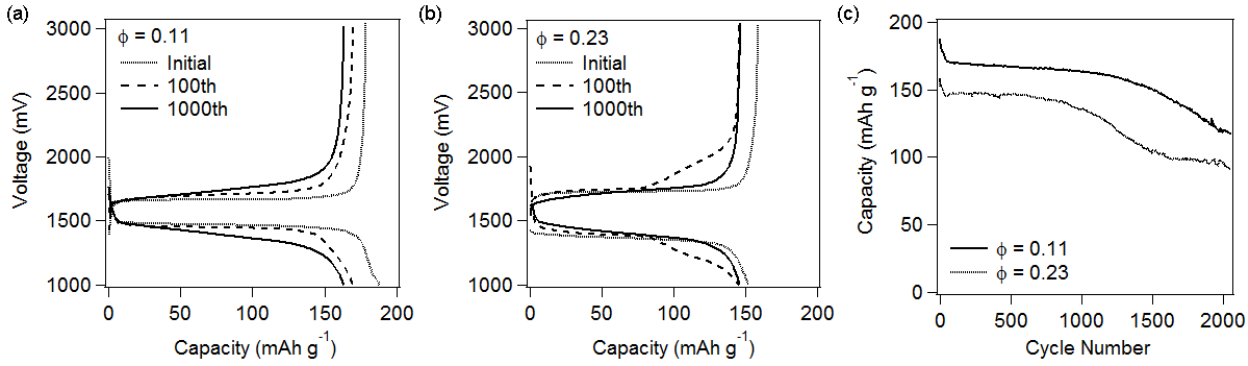

Figure 5: Galvanostatic charge-discharge profiles for Li/LTO half-cells containing SiO_2-PP-TFSI composite electrolytes at a fixed rate of 3C. (a) Charge and discharge voltage profiles for an electrolyte with ϕ=0.11 in the Initial, 100th and 1000th cycle; (b) Same as (a), except ϕ=0.23; (c) capacity versus cycle number for ϕ=0.11 and ϕ=0.23.